

DRAFT VERSION JULY 3, 2020

Typeset using L<sup>A</sup>T<sub>E</sub>X **preprint** style in AASTeX61

# THE STRUCTURE OF STELLAR DISKS IN ISOLATED LENTICULAR GALAXIES.<sup>a</sup>

OLGA K. SIL'CHENKO,<sup>1</sup> ALEXEI YU. KNIAZEV,<sup>2,3,1</sup> AND EKATERINA M. CHUDAKOVA<sup>1</sup>

<sup>1</sup>*Sternberg Astronomical Institute, M.V. Lomonosov Moscow State University, Universitetsky pr., 13, Moscow, 119991 Russia*

<sup>2</sup>*South African Astronomical Observatory, PO Box 9, 7935 Observatory, Cape Town, South Africa*

<sup>3</sup>*Southern African Large Telescope Foundation, PO Box 9, 7935 Observatory, Cape Town, South Africa*

Submitted to AJ

## ABSTRACT

We have obtained imaging data in two photometric bands,  $g$  and  $r$ , for a sample of 42 isolated lenticular galaxies with the Las Cumbres Observatory one-meter telescope network. We have analyzed the structure of their large-scale stellar disks. The parameters of surface brightness distributions have been determined including the radial profile shapes and disk thicknesses. After inspecting the radial brightness profiles, all the galaxies have been classified into pure exponential (Type I), truncated (Type II), and antitruncated (Type III) disks. By comparing the derived statistics of the radial profiles shapes with our previous sample of cluster S0s, we noted a prominent difference between stellar disks of S0s galaxies in quite rarefied environments and in clusters: it is only in sparse environments that Type II disks, with profile truncations, can be found. This finding implies probable different dynamical history of S0 galaxies in different environments.

*Keywords:* galaxies: elliptical and lenticular - galaxies: evolution - galaxies: formation  
- galaxies: structure.

Corresponding author: Olga Sil'chenko  
[olga@sai.msu.su](mailto:olga@sai.msu.su), [olgasil.astro@gmail.com](mailto:olgasil.astro@gmail.com)  
[olga@sai.msu.su](mailto:olga@sai.msu.su)  
[akniazev@sao.ac.za](mailto:akniazev@sao.ac.za)  
[artenik@gmail.com](mailto:artenik@gmail.com)

## 1. INTRODUCTION

The structure of a lenticular galaxy implies combination of a bulge and of a large-scale stellar disk, hence being quite similar to that of spiral galaxies. However, stellar disks of S0s are usually red and smooth and do not contain clumpy current star formation. Due to this (dis-)similarity lenticular galaxies are commonly thought to be descendants of spirals devoid of gas. It is easy to remove the gas from the galactic disk when a galaxy enters dense environments; many mechanisms for this purpose are proposed: ram pressure (Gunn & Gott 1972; Quilis, Moore, and Bower 2000) or static pressure (Cowie & Songaila 1977) by dense hot intergalactic medium, tidal effects – from the whole cluster (Byrd & Valtonen 1990), pair collisions (Spitzer & Baade 1951), harassment (Moore et al. 1996), slow fly-by (Icke 1985; Bekki & Couch 2011), starvation (Larson, Tinsley, and Caldwell 1980) etc.

But lenticular galaxies inhabit not only clusters, though they are the most numerous population there. A lot of S0s belong to loose groups, and some lenticulars are even quite isolated. It seems natural to suggest that they may have different evolutionary paths. Then the structure of their disks may reflect different dynamical evolution of S0s in different environments. The term ‘structure’ refers here to both radial and vertical surface-brightness distributions.

Concerning the radial structure of galactic stellar disks, it is presently established that the slope of their radial stellar surface-brightness decrease can be typically described by a piecewise exponential function. Now three main types of the radial brightness profiles are recognized: they can be fitted by a single-scale exponential over the whole extension of a stellar disk (Freeman 1970), or by an exponential law with truncation at some radius as firstly mentioned in Freeman (1970) and later classified as ‘breaks’ by Van der Kruit & Searle (1981), or with two exponential segments, the outer exponential law having a larger scalelength – so called antitruncated disks (Sil’chenko, Burenkov, and Vlasjuk 1998; Sil’chenko et al. 2003; Erwin, Beckman, and Pohlen 2005). After the SDSS statistics analysis by Pohlen & Trujillo (2006), these three types of surface-brightness profiles become to be numbered as follows: single-scale exponential disks are Type I, truncated disks are Type II, and antitruncated disks are Type III. The hot topic of discussion is if the shape of a stellar surface-brightness (density) profile is an initial condition of the galactic disk formation, or there exists some dynamical transitions between them. Firstly Erwin, Gutiérrez, and Beckman (2012), and later Pranger et al. (2017) and Sil’chenko, Kniazev, and Chudakova (2018), have reported a hint on the environment effect concerning the profile-shape statistics for early-type disk galaxies in clusters: there is a deficit of Type II profiles compensating by an excess of Type I profiles in these dense environments. Trying to give an evolutionary basis to this discovery, Clarke et al. (2017) proposed a dynamical mechanism to transform truncated disks into a single-scale exponential one during the infall of a galaxy into cluster environment: gas stripping by ram pressure and enhanced stellar radial migration together provide respective changes in a stellar disk structure. However, this mechanism works only for *gas-rich late-type* spirals and requires subsequent transformation of spirals into lenticulars. Concerning the origin of the most common, Type III disks of S0s, there were dynamical simulations proposing transformation of a single-scale exponential disk into an antitruncated one (e.g. Younger et al. 2007; Borlaff et al. 2014). Comprehensive cosmological simulations reveal the most violent dynamical evolution exactly for the Type-III disks: in the frame of LCDM-models they are formed by strong radial migration as well as by concentration of freshly accreted stars in their outermost parts (Ruiz-Lara et al. 2017).

Apart from the radial profile type, in this paper we consider another structure characteristics of galactic disks – their thickness. It is important to get estimates of the disk thicknesses for different disk radial-profile types because it will allow us to limit possible dynamical mechanisms shaping the large-scale stellar disk structure of real lenticular galaxies. In particular, dry minor mergers which have been elected by [Younger et al. \(2007\)](#) to form an antitruncated surface-density profile, are also expected to thicken stellar disks by increasing their vertical stellar velocity dispersion ([Walker, Mihos, and Hernquist 1996](#)). Observational estimates of galactic disk thicknesses are rare: individual estimates of stellar disk thickness were made directly only for galaxies seen edge-on (e.g. [Mosenkov, Sotnikova, and Reshetnikov 2010](#); [Mosenkov et al. 2015](#); [Comerón, Salo, and Knapen 2018](#)). However it is rather indirect to discuss radial and/or azimuthal structure of the galaxies seen strictly edge-on. We ([Chudakova & Sil’chenko 2014](#)) have invented a novel method allowing to estimate an individual thickness of an exponential (or piecewise exponential) stellar disk seen under arbitrary inclination; only strictly edge-on or strictly face-on disks cannot be analyzed by our method. With our method, we have already made some efforts, with the aim to compare disk thicknesses among the samples of various types of radial surface-brightness profiles for early-type disk galaxies in groups ([Chudakova & Sil’chenko 2014](#); [Sil’chenko, Kniazev, and Chudakova 2016](#)) and in clusters ([Sil’chenko et al. 2018](#)). In the present paper we continue to apply our method of estimating thicknesses in individual galactic disks to a sample of isolated S0 galaxies. In Section 2 we describe the sample, in Section 3 we give details of our observations and of our approach to the stellar disk structure characterization, in Section 4 we present our quantitative results and discuss them, and in Section 5 we conclude.

## 2. SAMPLE

The aim of our study is to inspect photometric structure of isolated lenticular galaxies. The criterium of isolation,  $II$ , has been defined by Karachentsev and Makarov with coauthors ([Makarov & Karachentsev 2011](#); [Karachentsev et al. 2011](#)); it is based on the consideration of mutual gravitational effect of all possible pairs of galaxies. The parent sample of rather isolated lenticular galaxies compiled by [Katkov \(2014\)](#) included 281 S0 galaxies within the volume of  $v_r < 4000 \text{ km s}^{-1}$  selected through the criterium of isolation index  $II > 2.5$ . This choice of  $II$  means that the mass of every sample galaxy has to be increased by a factor of 2.5 – or the nearest brighter galaxy mass has to be increased by a factor of 2.5 – to join the sample galaxy into a gravitationally bound ensemble with another galaxies. The consideration was limited by galaxies having the K-band magnitude fainter by 2.5 mag than our target galaxies. In other words, presently our galaxies are gravitationally unbound to any brighter galaxy or to any fainter galaxy within 10% of its mass. In the frame of our photometric project we have obtained imaging data for 42 southern-sky S0 galaxies from this parent sample; in order to be able to apply our method of disk thickness estimation we avoided strictly edge-on disks. The galaxies included into the sample are classified as S0 or S0/a in the NASA/IPAC Extragalactic Database (NED) or in the HyperLEDA. One galaxy, PGC 11756, is classified in HyperLEDA as E; but it is an obvious mistake since we have found that it lacks bulge (spheroid) at all. Additional check of the presence of a large-scale stellar disk in the galaxies selected for our analysis was made after deriving the surface brightness profiles by the method described in the next Section; we suggest that the main difference between S0 and an elliptical is the presence of a smooth large-scale disk. For every galaxy we started with a fit of the outer parts of the surface-brightness profiles by exponentials and proved that there exists at least one segment of a profile which lacks any systematic deviations

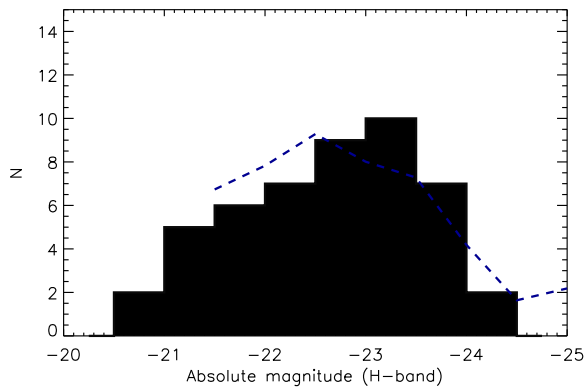


**Figure 1.** The distribution of the galaxy absolute magnitudes in the  $H$ -band for our sample; the  $M_H$  are taken from NED. The dashed line overposed represents the luminosity function of the volume-limited sample of early-type galaxies from Cappellari et al. (2011).

from the exponential law over a radial range of two exponential scalelengths. We took this criterium – namely, an exponential law validity over a two-scalelength radial range – from Freeman (1970): it was formulated in this classical work as a necessary property of exponential stellar disks. The range of luminosities of the isolated S0s in our study is found to extend from  $M_H = -21$  to  $M_H = -24.3$ . We have compared the distribution of the NIR absolute magnitudes of our galaxies (Fig. 1) with the luminosity function of the volume-limited sample of nearby early-type galaxies from Cappellari et al. (2011) and have assured that they agree well: the Kolmogorov-Smirnov (K-S) test has shown the difference statistics of  $d_{max} = 0.072$ , or  $\lambda = 0.42$ , that means that the distributions are the same with the probability greater than 99%. With our sample of isolated lenticulars we probe all the luminosity range of non-dwarf S0 galaxies, so we may hope that our sample of isolated S0s is representative.

We want to compare the results obtained here for the sample of isolated lenticular galaxies to those for the sample of 60 cluster lenticular galaxies which have been studied by us earlier (Sil'chenko et al. 2018). The cluster S0s, in the same range of luminosities, were taken by us in 8 southern clusters of galaxies, spanning a range of masses (X-ray luminosities) but all being not too far from us – within  $D = 71$  Mpc.

### 3. OBSERVATIONS AND DATA ANALYSIS

The photometric observations of the sample of isolated S0s have been undertaken with the Las Cumbres Observatory (LCO) robotic telescope network (Brown et al. 2013) during 2016–2018. The LCO network includes two 2-m telescopes, ten 1-m telescopes, and ten 40-cm telescopes – in total 22 telescopes distributed among 7 different observatories. All our observations were done with the LCO one-meter telescopes equipped by standard Sinistro cameras intended to acquire image frames. Such camera contains a  $4000 \times 4000$  CCD. With the physical pixel size of  $15 \mu\text{m}$  and standard  $1 \times 1$  binning, we get a scale of 0.389 arcsec per pixel, and every single frame covers an area of  $26 \times 26$  arcmin. Each Sinistro camera is equipped by 21 different filters, of which we used the  $g$  and  $r$  broad-band filters of the Sloan survey photometric system. The log of the observations is given in the Appendix.

During the observations, there were no dedicated exposures of photometric standards, so we calibrated our images by three different ways:

- by using the HyperLEDA<sup>1</sup> aperture photometry data – the Johnson-Cousins  $B(V)R$  aperture measurements for every galaxy, mostly based on the compilations of the photometric survey of the southern sky (Lauberts & Valentijn 1989) which we transformed into the  $gr$ -system with the interrelations found by Jordi, Grebel, and Ammon (2006);
- for the galaxies covered by the SDSS survey (NGC 270, NGC 1656, NGC 6014, UGC 5745) we have used the  $gr$ -photometry of nearby stars from the SDSS/DR9 public data archive (Ahn et al. 2012) as standards;
- also we have used  $gr$ -photometry of the neighboring stars from the Pan-STARRS1/DR1 (Chambers et al. 2016; Flewelling et al. 2016) public data archive as standards for the galaxies with declinations larger than  $-30^\circ$ .

The images were initially reduced by the LCO pipeline which performs bias subtraction and flat-fielding of individual frames. Then we co-added the images made in the same filters for every galaxy, proceeding cosmic hit cleaning simultaneously, and estimated the sky background distributions in the aggregate frames. The sky background level for every galaxy was estimated over several large, by  $51 \times 51$  pixels, empty square areas, taken in at least eight different directions from the galaxy. Then the sky background estimates were averaged, or, in the case of detected gradient over the frame, interpolated linearly onto the galaxy position.

After obtaining the flat-fielded and sky-subtracted images, we made then isophotal analysis for every galaxy by using the analog of the ELLIPSE/IRAF algorithm and derived radial profiles of the isophote ellipticities and major-axis position angle by going from the galaxy center outward with the logarithmic brightness step of 0.05. By assuming that the large-scale stellar disks of our S0s were flat and did not suffer warps, for every galaxy we fixed a radius where the isophote ellipticity stopped to rise steeply and reached a plateau. We suggest that the flat disk dominates in the total surface brightness of an outer region of a galaxy beyond this radius. To derive azimuthally averaged surface-brightness profiles of the disks, we selected the parameters of the elliptical apertures intending to characterize a round disk projection onto the sky plane, by exploring the isophote ellipticity and major-axis position angle found just at this radius marking the rise of the disk-dominated area. Then we averaged the surface brightnesses over the elliptical rings by going outward with some steps along the radius. Finally the azimuthally averaged surface-brightness profiles of the stellar disks were obtained. For the innermost regions, where the ellipticity and major-axis position angle of the isophotes changed strongly along the radius, we averaged the surface brightness in the elliptical rings with the orientation and shape modifying radially in accordance with the results of the isophote analysis. After deriving azimuthally averaged surface-brightness profiles, we started to fit them by an exponential function selecting initially the radial range between the outermost point exceeding the sky level by an rms sky-level scatter value and the innermost radius where the profile points still obey to the exponential law fitted. The quality of the fit was taken to be good if the rms scatter of the points around the fitting line was found to be within typical errors of the individual measurements. If we found an inner radius where the azimuthally averaged surface-brightness profile started to deviate systematically up or down from the fitted exponential law by a value exceeding the rms scatter of the observational points around the fitted exponential law and if this radius was

<sup>1</sup> <http://leda.univ-lyon1.fr>

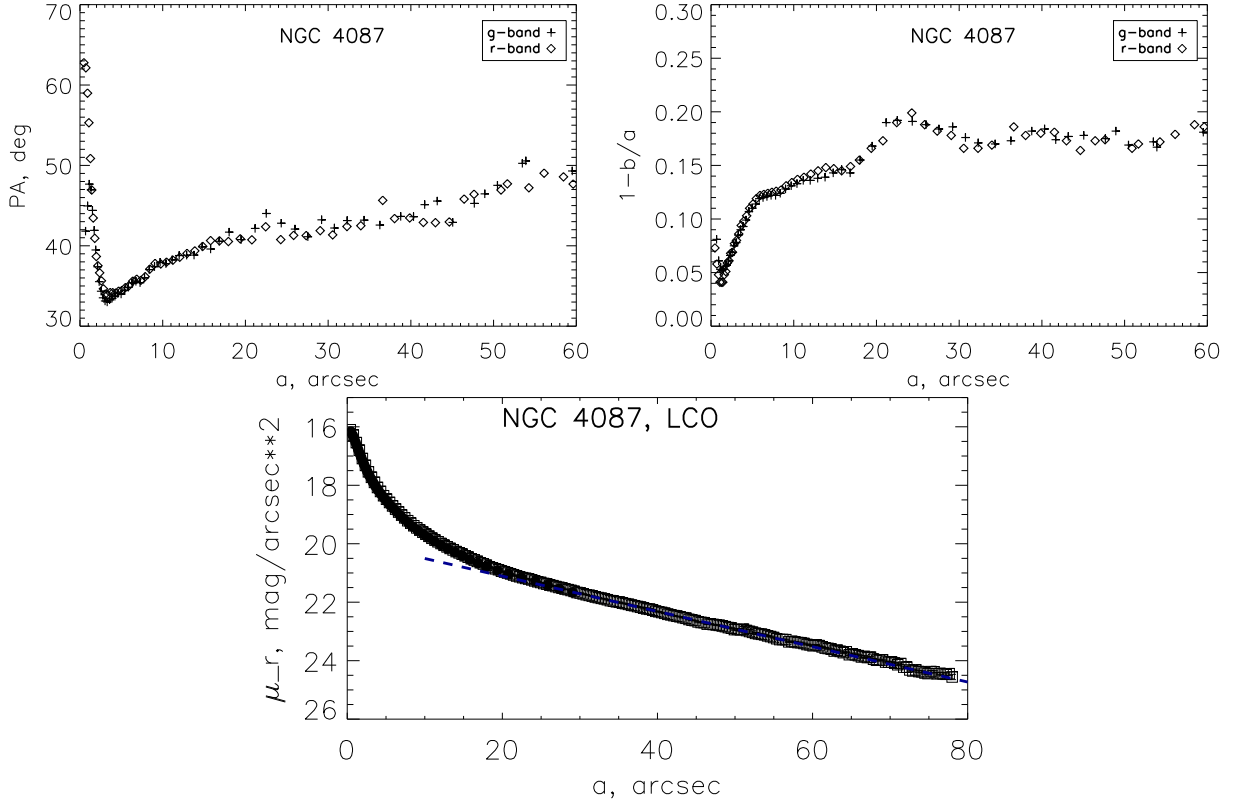


**Figure 2.** An example of a single-scale exponential surface-brightness profile (Type I): NGC 4087. The upper row shows the results of the isophote analysis in two bands, the bottom plot is an azimuthally-averaged surface-brightness profile in the  $r$ -band. In the surface-brightness profile the black dots present the measurements azimuthally averaged with running ellipticity and orientation of the elliptical aperture, while open squares with error bars – those with fixed orientation of the elliptical aperture corresponding to the line-of-nodes position angle and inclination of the disk (see the text).

still within the disk-dominated radial range characterizing by the stable high isophote ellipticity, we concluded that the profile is not of the Type I, and fitted another exponential segment into the inner part of the azimuthally averaged surface-brightness profile. By applying this procedure to the whole sample, we have divided the total galaxy list into three subsamples: the S0s with Type-I profiles, the S0s with Type-II profiles, and the S0s with Type-III profiles. Figures 2, 3, and 4 demonstrate some examples of all three types of the disk surface-brightness profiles in our sample.

[t]

**Table 1.** The galaxies studied photometrically with the LCO network.

Galaxy	Type <sup>a</sup>	$M_H^a$	$R_{25}''^b$	Profile type	Bar/ring?	Color features
ESO 003-001	(R <sub>1</sub> )SB(rs)0/a	−23.74	46.5	III	bar, ring	blue knot in 5'' to NW
ESO 040-002	SA0 <sup>−</sup> :	−23.98	39	III	...	...
ESO 052-014	(R' <sub>2</sub> )SB(s)0/a	−22.02	37	III	bar, arms	dust lane

*Table 1 continued on next page*



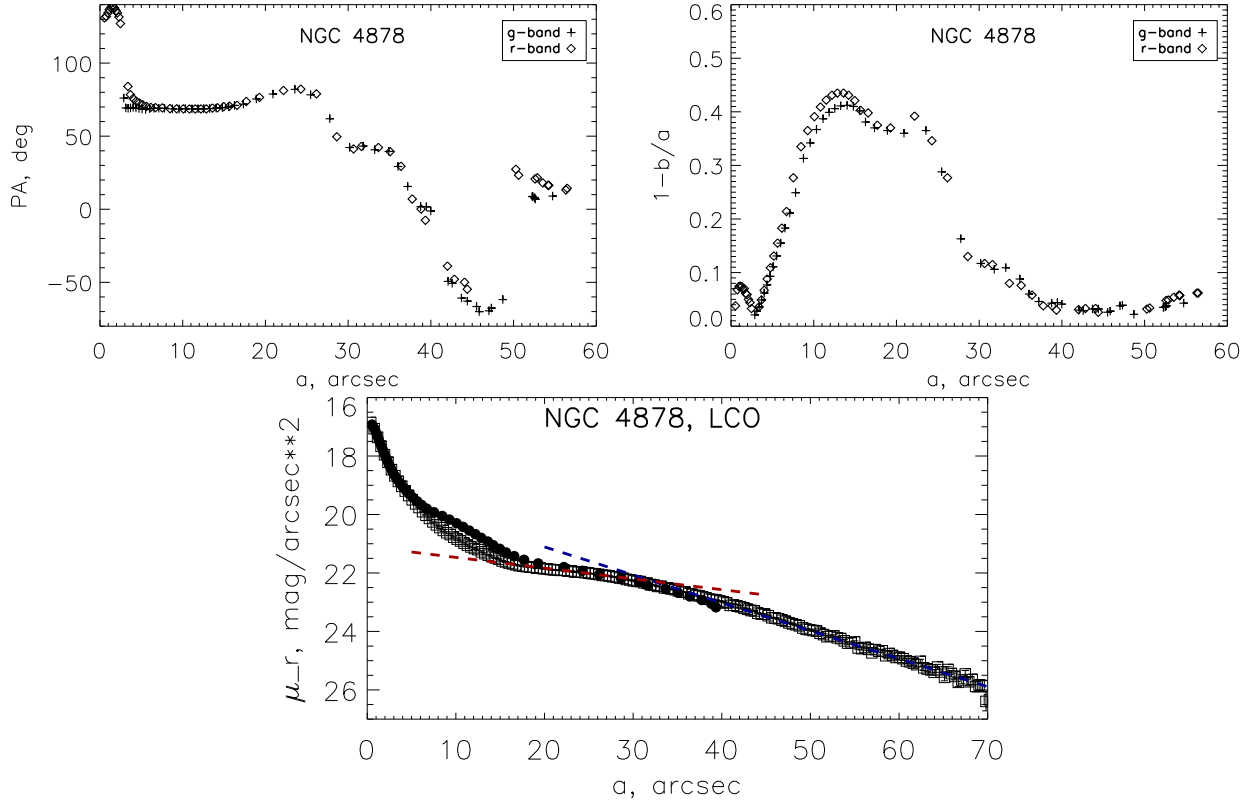


**Figure 3.** An example of a truncated piecewise exponential surface-brightness profile (Type II): NGC 4878. The upper row shows the results of the isophote analysis in two bands, the bottom plot is an azimuthally-averaged surface-brightness profile in the  $r$ -band. In the surface-brightness profile the black dots present the measurements azimuthally averaged with running ellipticity and orientation of the elliptical aperture, while open squares with error bars – those with fixed orientation of the elliptical aperture corresponding to the line-of-nodes position angle and inclination of the disk (see the text).

**Table 1** (*continued*)

Galaxy	Type <sup>a</sup>	$M_H^a$	$R_{25}^b$	Profile type	Bar/ring?	Color features
ESO 069-001	(L)SAB(rl)0 <sup>0</sup>	-23.32	40	II	bar	...
ESO 235-051	SB(s)0 <sup>+</sup>	-21.37	41.5	I	bar, arms	blue bulge
ESO 265-033	S0?	-23.44	40	II	boxy bulge, ansae	inclined dust disk
ESO 269-013	(R)SB(r)0 <sup>+</sup>	-24.01	42	III	bar, rings	two blue rings
ESO 274-017	S0/a(LEDa)	-22.34	27	III	stars projected?	...
ESO 316-013	S0	-23.62	27	I	bar	central red semiring
ESO 324-029	SAB(r)0 <sup>+</sup>	-23.47	72	III-II	broad inner ring	inner blue ring
ESO 446-049	SA(r)0 <sup>+</sup> :	-23.15	42	III	outer ring	central oval red ring
ESO 469-006	S0	-21.21	27	III	...	dust lane

Table 1 continued on next page

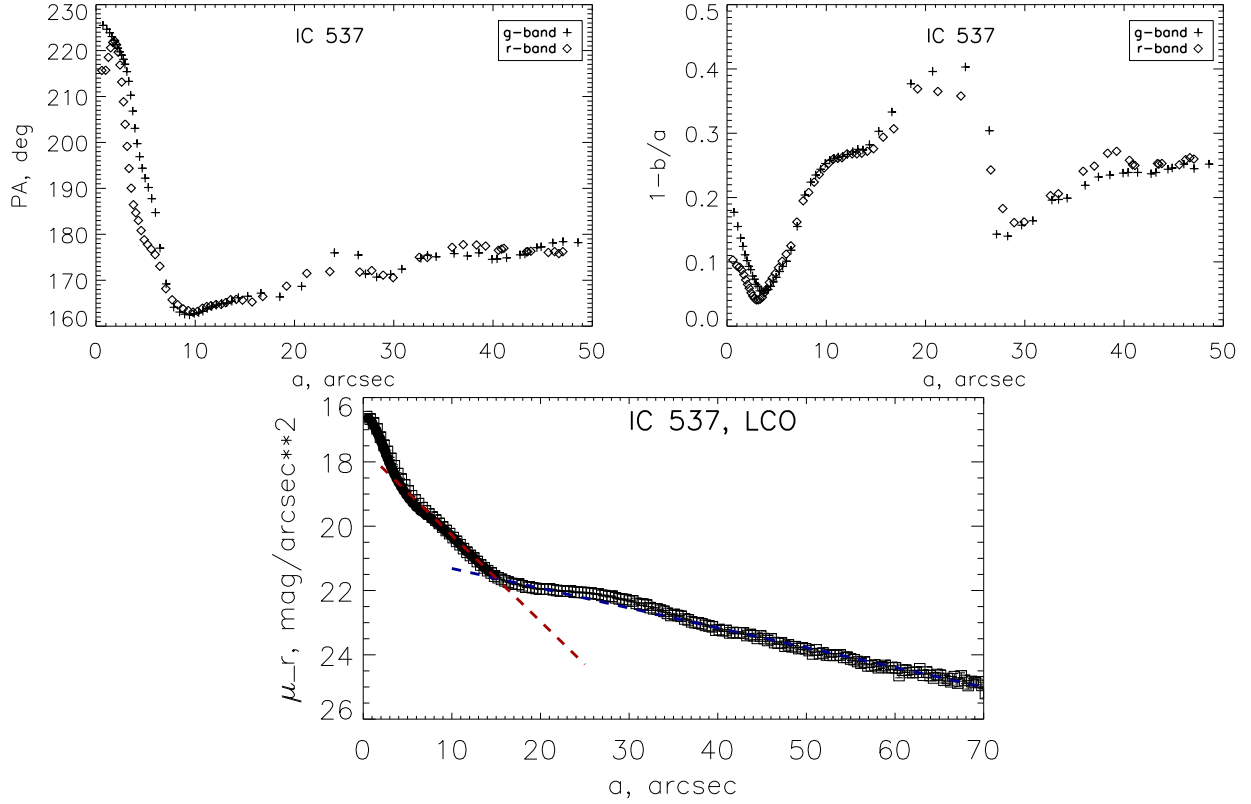


**Figure 4.** An example of a two-tiered (antitruncated) exponential surface-brightness profile (Type III): IC 537. The upper row shows the results of the isophote analysis in two bands, the bottom plot is an azimuthally-averaged surface-brightness profile in the  $r$ -band. In the surface-brightness profile the black dots present the measurements azimuthally averaged with running ellipticity and orientation of the elliptical aperture, while open squares with error bars – those with fixed orientation of the elliptical aperture corresponding to the line-of-nodes position angle and inclination of the disk (see the text). The outer segment of the disk contains a ring at the radius of  $30''$ .

**Table 1** (*continued*)

Galaxy	Type <sup>a</sup>	$M_H^a$	$R_{25}, ''^b$	Profile type	Bar/ring?	Color features
ESO 486-038	S0	-22.60	33	III	...	blue star projected
ESO 496-003	S0	-22.80	34.5	I	broad outer ring	red nucleus
ESO 506-011	S0	-22.80	39	I	...	red nucleus
ESO 508-033	S0?	-22.38	24	III	...	blue nucleus
ESO 545-040	SA(rs)0 <sup>0</sup> ?	-20.94	47.5	III	boxy bulge	blue semiring, red nucleus
ESO 563-024	S0	-23.58	34	I	...	red nucleus
ESO 603-029	(L)SAB0 <sup>0</sup>	-21.92	31	I	broad ring	asym. dust lane
IC 276	S0 <sup>0</sup> pec	-22.69	50	III	...	red nucleus, blue bulge
IC 537	(R)S0/a?	-23.83	39.5	III	bar, outer ring	inner red semiring

*Table 1 continued on next page*



**Table 1** (*continued*)

Galaxy	Type <sup>a</sup>	$M_H^a$	$R_{25},''^b$	Profile type	Bar/ring?	Color features
IC 4913	SA0–	–23.38	48	I	...	red nucleus
NGC 270	S0 <sup>+</sup>	–23.29	53	III	shells	asym. red arm and dust lane
NGC 324	S0(LED A)	–23.06	44	I	...	blue bulge, red nucleus
NGC 1656	S0 <sup>+</sup> pec:	–23.39	52	III	bar	red thin bar, blue bulge
NGC 4087	SA0 <sup>–</sup> :	–24.30	60	I	...	red nucleus
NGC 4878	SB(r)0 <sup>+</sup>	–23.98	45	II	bar, outer ring	...
NGC 5890	SA(rl)0 <sup>0</sup>	–22.44	46.5	I	stellar arms	blue nucleus, red dust arc
NGC 6014	S0	–23.90	52	II	shells	blue nucleus, red patches
NGC 7007	SA0 <sup>–</sup>	–23.30	102	III	small bar	east-west color asymmetry
NGC 7208	SAB0 <sup>0</sup> ?	–21.64	27	III	stellar arms, merger	blue embedded object
PGC 11756	E(LED A)	–22.23	22	II	ansae	inner blue ring
PGC 16688	S0(LED A)	–21.70	27	III	bar	asym. dust lane
PGC 34728	SA0 <sup>–</sup> pec	–22.51	50	III	...	...
PGC 35771	S0/a(LED A)	–23.25	30	II	bar, arms	red spirals, blue inclusion
PGC 46474	S0/a(LED A)	–21.04	35	III	ring	blue patchy center
PGC 52002	S0(LED A)	–22.53	29	I	...	red nucleus
PGC 58114	S0	–21.16	31(K)	III	bar	asym. dust lane
PGC 63536	SA(r)0 <sup>–</sup>	–21.30	42	III	...	red nucleus
PGC 68401	(R')SB(rs)0 <sup>+</sup>	–21.91	60	III	ring	asym. blue outer ring/tail
UGC 3097	S0	–21.71	24	III	bar	blue disk, asym. dust lane
UGC 5745	SB(rs)0 <sup>+</sup>	–21.54	36	I	bar, ring	asym. dust lane, red arms

<sup>a</sup>Mostly from NED; but some data taken from HyperLEDA (Makarov et al. 2014) are marked by ‘(LEDA)’.

<sup>b</sup>Mostly the optical radii are taken from HyperLEDA (Makarov et al. 2014); but some NIR radii taken from NED are marked by ‘(K)’.

The relative thicknesses of the disks characterizing the ratio of the vertical and radial scalelengths were calculated by our novel method described in details by Chudakova & Sil’chenko (2014). The careful testing of the method and determination of the boundaries of its applicability can be found in Chudakova (2019). In a few words, we used the analysis of the projection effects for an oblate ellipsoid with the axes  $a_1 = a_2 > a_3$  made by Hubble (1926). If we look at the intrinsically round, infinitely thin disk projected onto the sky plane under the inclination  $i$  (here we fix  $i = 90^\circ$  for edge-on disks), we would see an ellipse with the axis ratio of  $b/a = \cos i$ . If the disk is not infinitely thin and can be described by an oblate ellipsoid with the vertical-to-radial axis ratio of  $q$ , then  $\cos^2 i = \frac{(b/a)^2 - q^2}{1 - q^2}$ . The latter equation enables us to calculate the relative disk thickness  $q$ , if we invent a possibility to measure independently the inclination  $i$  and the isophote axis ratio  $b/a$ . The latter parameter, a visible axis ratio, is provided by the isophote analysis. As for the former parameter, we can obtain

it directly from the 2D surface photometry if we assume that the disk under consideration has an exponential radial brightness profile. Indeed, the exponential scalelength for a given galactic disk can be used as a standard rule, characterizing projection effects. Its measurements, taken under different azimuth angles, would follow a pure cosine law and would vary from  $h$  along the major axis to  $h \cos i$  along the minor axis. The knowledge of the 'projected  $h$ ' azimuthal changes provides an independent estimate of the inclination  $i$ . We split commonly a full galaxy image into 20 sectors, with 18-degree opening angle each, and measure surface-brightness profiles within each of them. These surface-brightness profiles are fitted by exponentials, and the on-plane azimuthal distribution of the 20 (projected) scalelengths obtained in such a way is approximated by an ellipse. Just this scalelength ellipse must have an axis ratio equal to  $\cos i$  so giving us a possibility to determine the disk inclination. Then, having in hands the disk inclination  $i$  and the isophote ellipticity, we can estimate of the disk relative thickness. Namely, by measuring the isophote ellipticity  $e_I$  and the ellipticity of the azimuthal distribution of the projected exponential scalelengths  $e_h$ , we immediately derive the exponential disk relative thickness from the following expression:

$$q = \sqrt{1 - \frac{2e_I - e_I^2}{2e_h - e_h^2}}. \quad (1)$$

## 4. THE RESULTS AND DISCUSSION

### 4.1. Variety of the isolated S0s

Table 1 lists all 42 galaxies which we have analyzed, with specifying also the type of the disk surface-brightness profile which we have determined, and with attached notes about additional structure details and color features seen in the  $g - r$  maps. The presence of a bar was recognized by us through visual morphological classification, or when the isophote ellipticity profile had a distinct local maximum exceeding the outer ellipticity level related to the disk spatial orientation. The existence of a ring is fixed through the visual inspection of the surface-brightness profiles; the rings can be or not to be highlighted by the color. The color distributions demonstrate many small-scale features: just isolated S0s are not so smooth as we are in the habit of thinking. The low-luminosity S0s possess sometimes blue nuclei; moreover, the low-luminosity isolated S0s are often looking like merger remnants (Fig. 5). Among the galaxies of all luminosities the blue rings of various sizes or circumnuclear red (dust) lanes can also be noted. We show some typical cases of the inhomogeneous color distributions in our galaxies in Fig. 6.

We give the results of our analysis for the radial and vertical structures of the  $r$ -band images of the galactic disks in the Table 2 for the brightness profiles of Type I, in the Table 3 for the brightness profiles of Type II, and in the Table 4 for the brightness profiles of Type III, correspondingly. The radial surface-brightness profile parameters – central surface brightnesses  $\mu_0$  and exponential scalelengths  $h$  – are calculated by fitting the profiles with exponential functions in the radius ranges noted in the Tables. Following Freeman (1970), we tried to use the radius ranges which were at least twice larger than the fitted exponential scalelengths, but for the Type II profiles the inner segments were often shorter, being of order of one exponential scalelengths. The  $\mu_0$ 's given in the Tables are not corrected for the intrinsic dust; only Galactic extinction provided by NED is taken into account. The relative thicknesses of the stellar disks,  $q$ , are also given in the Tables; they have been calculated

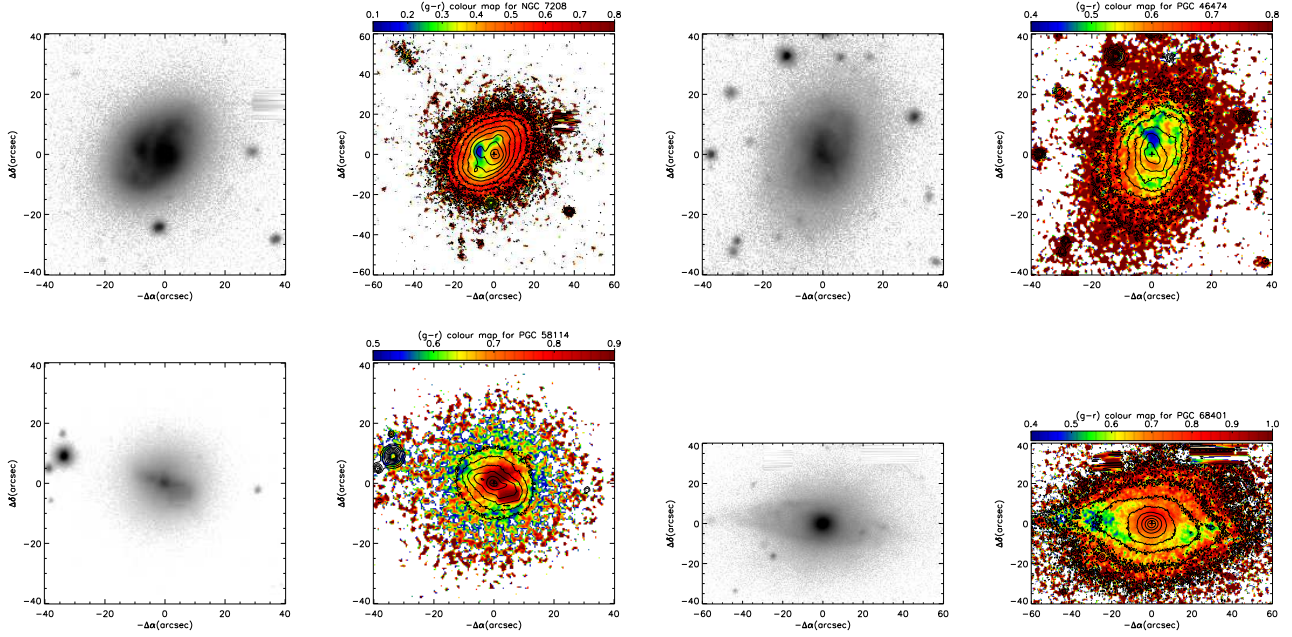


**Figure 5.** Some examples of the merger signatures in the dwarf isolated S0s. In every pair of plots the left one shows the  $r$ -band map, in logarithmic flux scale, and the right one – the color map, of  $g - r$ .

only for the high signal-to-noise images, not contaminated by foreground stars, and which are also far from edge-on or face-on orientation. The relative thicknesses  $q$  of the stellar disks, characterizing the ratio of the vertical and radial scalelengths, are presented in the Table 2 for the entire single-scale exponential disks, but in the Table 3 and Table 4 only for the inner segments of the truncated and antitruncated disks.

#### 4.2. Radial structure of the S0 disks in various environments

Erwin et al. (2012) were the first who reported about the difference between typical structure of the S0 disks in the field and in a cluster: they had analyzed radial structure of 24 S0 galaxies – members of the Virgo cluster – and had concluded that the statistics of the surface-brightness profile types in the cluster differed significantly from that in the field. They had not found any Type-II profiles in the Virgo S0s at all while in the field a quarter of all S0s demonstrated truncated stellar disks (Erwin et al. 2008; Gutiérrez et al. 2011). The following fractions of the profile types in the Virgo were reported by Erwin et al. (2012):  $46\% \pm 10\%$  of the Type I,  $0\% \pm 4\%$  of the Type II, and the remaining 54% profiles of the Type III. Our results (Sil’chenko et al. 2018) on 60 lenticular galaxies in 8 southern clusters were: 27 S0s of Type I –  $45\% \pm 6\%$ , 3 S0s of Type II –  $5\% \pm 3\%$  (the errors indicated the root square of the binomial distribution variance), the rest half of all S0s in clusters – of Type III. We pointed out then that our results were completely consistent with the statistics of the Virgo S0s reported by Erwin et al. (2012) and also differed from the field statistics where  $26\% \pm 6\%$  of Type I and  $28\% \pm 6\%$  of Type II were reported by Erwin et al. (2012). Our present results for the quite isolated S0s are: 12 S0s of Type I –  $28\% \pm 7\%$ , 7 S0s of Type II –  $17\% \pm 6\%$ , 23 S0s of Type III –  $55\% \pm 8\%$  (the fraction errors are again estimated as the root square of the binomial distribution variance). We conclude that the profile type distributions among the isolated S0s does not differ from that for the field, while mostly group S0s were reported by Erwin et al. (2008); Gutiérrez et al. (2011).



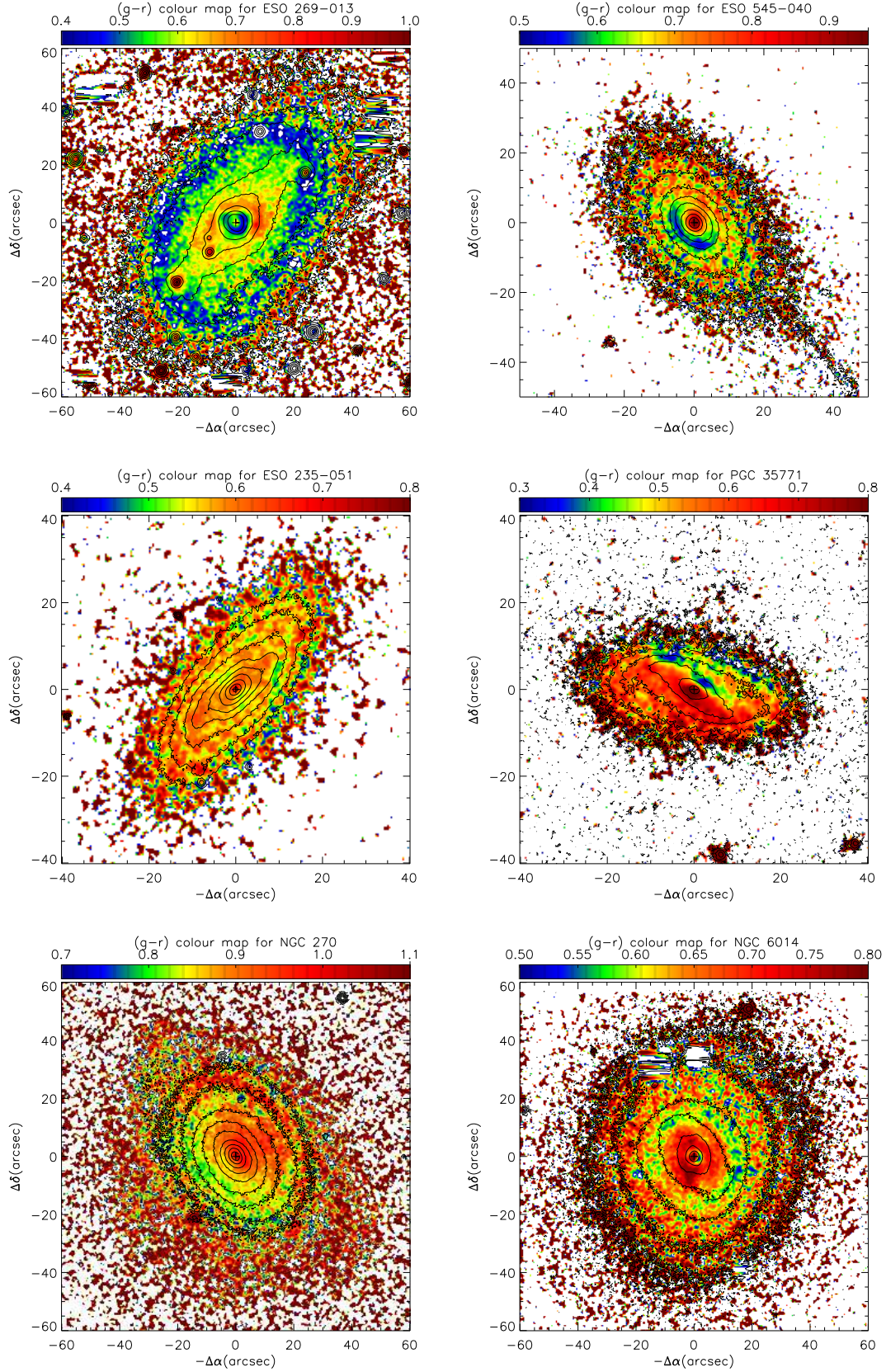


**Figure 6.** Some examples of the color structures: *upper row* – circumnuclear and inner blue rings, *middle row* – red nuclear spiral arms, *bottom row* – shells, both reddish or blue. The isophotes overposed represent the  $r$ -band surface brightness levels.

**Table 2.** Parameters of the Type-I disks

Galaxy	Radius range, ''	$\mu_0(r)$	$h_r$ , ''	$h_r$ , kpc	q
ESO 235-051	10–40	19.2	$8.6 \pm 0.0$	$1.2 \pm 0.0$	$0.298 \pm 0.006$
ESO 316-013	20–40	19.2	$10.9 \pm 0.01$	$2.8 \pm 0.0$	
ESO 496-003	8–25	18.8	$8.0 \pm 0.0$	$1.4 \pm 0.0$	$0.536 \pm 0.001$
ESO 506-011	18–45	20.1	$9.0 \pm 0.1$	$2.1 \pm 0.0$	
ESO 563-024	20–50	20.3	$13.1 \pm 0.0$	$2.6 \pm 0.0$	
ESO 603-029	8–33	18.5	$6.0 \pm 0.05$	$1.20 \pm 0.01$	$0.303 \pm 0.011$
IC 4913	10–43	20.0	$11.23 \pm 0.01$	$2.5 \pm 0.0$	$0.40 \pm 0.02$
NGC 324	20–60	19.3	$9.9 \pm 0.0$	$2.1 \pm 0.0$	$0.224 \pm 0.043$
NGC 4087	25–75	19.7	$18.0 \pm 0.0$	$4.3 \pm 0.0$	$0.548 \pm 0.026$
NGC 5890	10–60	19.3	$12.48 \pm 0.01$	$1.9 \pm 0.0$	$0.47 \pm 0.02$
PGC 52002	15–48	19.9	$8.62 \pm 0.01$	$1.6 \pm 0.0$	$0.190 \pm 0.015$
UGC 5745	10–50	19.1	$8.05 \pm 0.00$	$0.7 \pm 0.0$	

**Table 3.** Parameters of the Type-II disks

Galaxy	Inner disk						Outer disk			
	Radius range, ''	$\mu_0(r)$	$h_r$ , ''	$h_r$ , kpc	q	$\mu_{brk}$	Radius range, ''	$\mu_0(r)$	$h_r$ , ''	$h_r$ , kpc
ESO 069-001	12–28	19.1::	$8.23 \pm 0.16$	$1.93 \pm 0.04$		22.4::	27–34	17.1::	$5.27 \pm 0.06$	$1.24 \pm 0.01$
ESO 265-033	9–19	19.3	$9.1 \pm 0.2$	$2.65 \pm 0.06$	0.18	21.64	20–34	18.3	$6.39 \pm 0.14$	$1.86 \pm 0.04$
ESO 324-029	40–60	19.7	$23.76 \pm 0.03$	$3.82 \pm 0.00$	0.23	22.6	60–105	18.0	$15.02 \pm 0.02$	$2.42 \pm 0.00$
NGC 4878	16–30	21.0	$29.51 \pm 0.06$	$8.03 \pm 0.02$		22.2	37–67	19.1	$11.36 \pm 0.13$	$3.09 \pm 0.04$
NGC 6014	22–34	20.5	$16.31 \pm 0.01$	$2.67 \pm 0.00$	0.59	23.1	35–65	19.8	$12.88 \pm 0.01$	$2.1 \pm 0.0$
PGC 11756	1–8	18.7	$7.8 \pm 0.15$	$2.25 \pm 0.04$		19.8	10–25	17.6	$3.77 \pm 0.03$	$1.1 \pm 0.0$
PGC 35771	6–16	19.9	$9.0 \pm 0.2$	$2.66 \pm 0.06$	0.33	21.0	20–32	19.5	$6.54 \pm 0.31$	$1.95 \pm 0.09$

If we compare the present statistics for the isolated S0s with the results obtained by us with the same methods over the similar data for the cluster S0s in our previous work (Sil’chenko et al. 2018), we confirm that the main difference between the cluster S0s and S0s in more rarefied environments is the depletion of Type II profile occurrence in clusters and its noticeable presence in sparse environments. The occurrence of Type III profiles in S0 galaxies does not depend on environments – they constitute about a half everywhere. All this statistics is visualized in Fig. 7.

#### 4.3. Vertical structure of the S0 disks

**Table 4.** Parameters of the Type-III disks

Galaxy	Inner disk						Outer disk			
	Radius, ''	$\mu_0(r)$	$h_r$ , ''	$h_r$ , kpc	$q$	$\mu_{brk}$	Radius, ''	$\mu_0(r)$	$h_r$ , ''	$h_r$ , kpc
ESO 003-001	11–30	19.1	$9.0 \pm 0.0$	$2.4 \pm 0.0$		22.9	30–47	20.7	$15.3 \pm 0.6$	$4.05 \pm 0.16$
ESO 040-002	10–28	19.8(g)::	$10.5 \pm 0.0$	$2.1 \pm 0.0$	$0.61 \pm 0.02$	22.6(g)::	30–48	20.8(g)::	$16.4 \pm 0.4$	$3.26 \pm 0.08$
ESO 052-014	9–27	19.1	$8.2 \pm 0.1$	$1.6 \pm 0.0$		22.8	27–50	20.8	$15.2 \pm 0.4$	$3.0 \pm 0.1$
ESO 269-013	15–50	20.2	$16.16 \pm 0.02$	$4.28 \pm 0.01$	$0.53 \pm 0.01$	23.8	50–85	21.1	$21.5 \pm 0.5$	$5.7 \pm 0.1$
ESO 274-017	5–11	18.6	$3.8 \pm 0.08$	$0.87 \pm 0.02$		21.9	12–22	20.3	$7.8 \pm 0.3$	$1.78 \pm 0.07$
ESO 446-049	6–17	18.7	$6.4 \pm 0.05$	$1.7 \pm 0.0$	$0.43 \pm 0.02$	21.15	20–55	19.6	$10.15 \pm 0.005$	$2.70 \pm 0.00$
ESO 469-006	5–13	19.0	$4.11 \pm 0.04$	$0.73 \pm 0.01$	$0.105 \pm 0.011$	22.5	15–32	20.0	$6.0 \pm 0.1$	$1.07 \pm 0.02$
ESO 486-038	15–40	20.5	$11.1 \pm 0.0$	$3.0 \pm 0.0$		24.8	42–57	22.3	$19 \pm 3$	$5.2 \pm 0.8$
ESO 508-033	4–13	18.0	$3.95 \pm 0.03$	$0.94 \pm 0.01$	$0.22 \pm 0.01$	21.9	16–28	19.6	$6.54 \pm 0.01$	$1.55 \pm 0.00$
ESO 545-040	15–45	20.1	$13.4 \pm 0.0$	$1.1 \pm 0.0$	$0.35 \pm 0.01$	23.7	45–60	21.0	$17.9 \pm 1.3$	$1.5 \pm 0.1$
IC 276	12–25	17.7	$7.0 \pm 0.05$	$1.26 \pm 0.01$		21.85	30–60	19.8	$14.1 \pm 0.2$	$2.54 \pm 0.04$
IC 537	5–15	17.5	$4.05 \pm 0.04$	$1.10 \pm 0.01$	$0.22 \pm 0.02$	21.5	18–64	20.6	$17.66 \pm 0.02$	$4.82 \pm 0.01$
NGC 270	12–25	19.3	$10.3 \pm 0.1$	$2.33 \pm 0.02$	$0.46 \pm 0.02$	22.3	35–70	20.8	$20.7 \pm 0.0$	$4.7 \pm 0.0$
NGC 1656	15–30	19.4	$12.00 \pm 0.01$	$2.9 \pm 0.0$	$0.54 \pm 0.02$	22.3	35–80	20.6	$20.34 \pm 0.02$	$4.96 \pm 0.00$
NGC 7007	20–40	19.2	$12.57 \pm 0.01$	$2.43 \pm 0.00$	$0.26 \pm 0.01$	23.0	45–75	20.8	$21.9 \pm 0.6$	$4.23 \pm 0.12$
NGC 7208	9–20	18.0	$4.50 \pm 0.04$	$0.70 \pm 0.01$	$0.44 \pm 0.02$	23.5	28–48	21.4	$11.44 \pm 0.43$	$1.78 \pm 0.07$
PGC 16688	5–12	19.1	$4.36 \pm 0.05$	$0.85 \pm 0.01$	$0.554 \pm 0.026$	21.9	12–24	20.0	$6.5 \pm 0.1$	$1.27 \pm 0.02$
PGC 34728	9–24	20.0	$8.55 \pm 0.15$	$2.3 \pm 0.04$		22.4	28–54	20.9	$13.6 \pm 0.6$	$3.6 \pm 0.2$
PGC 46474	3–18	19.3	$6.4 \pm 0.04$	$1.22 \pm 0.01$	$0.36 \pm 0.01$	22.75	20–40	20.8	$11.28 \pm 0.15$	$2.14 \pm 0.03$
PGC 58114	3–14	18.1	$4.40 \pm 0.03$	$0.46 \pm 0.00$		21.8	16–30	20.2	$10.3 \pm 0.2$	$1.07 \pm 0.02$
PGC 63536	13–28	19.9	$10.34 \pm 0.16$	$1.24 \pm 0.02$	$0.41 \pm 0.02$	22.9	36–52	21.1	$17.3 \pm 1.6$	$2.08 \pm 0.19$
PGC 68401	13–28	20.4	$13.07 \pm 0.01$	$2.10 \pm 0.00$	$0.49 \pm 0.02$	23.25	40–75	21.9	$27.36 \pm 0.05$	$4.40 \pm 0.01$
UGC 3097	6–16	18.8	$5.12 \pm 0.04$	$1.18 \pm 0.01$	$0.43 \pm 0.02$	21.65	20–33	19.4	$6.5 \pm 0.25$	$1.50 \pm 0.06$

The novel point of our photometric analysis is individual estimates of the stellar disk relative thicknesses expressed in the terms of [Hubble \(1926\)](#)’s parameter  $q$  – we present them in the Table 2, the Table 3, and the Table 4, for the inner segments of the piecewise exponential disks.

Figure 8 presents the distributions of the relative disk thicknesses for the Type-I disks (*left*) and for the inner segments of the Type-III disks (*right*); in this Figure we compare the thickness distributions for the isolated S0s (top plots) and for the cluster S0s (bottom plots), the latter obtained in our previous work ([Sil’chenko et al. 2018](#)). The median thickness of the isolated Type-I disks is 0.35, while the median thickness of the cluster Type-I disks is 0.31. The cause of this formal dissimilarity is the fact that the thickness distribution of the isolated S0s Type-I disks includes a few very thick,  $q \approx 0.5$ , disks which are absent in clusters. However, the Type-I sample is small hence we cannot make any certain conclusions about its thickness distribution. More certain difference is demonstrated by the inner Type-III disks: without pseudobulges, defined as having  $q > 0.5$ , the mean thickness of the cluster S0 disks is  $0.25 \pm 0.02$ , while the isolated S0 disks have  $0.35 \pm 0.03$ . The sample of the inner Type-III disks with the measured thicknesses is large enough, so we can apply the K-S test. By considering the full  $q$  distribution for the isolated inner Type-III disks in comparison with the analogous distribution for the cluster S0s, we find that the K-S statistics is  $\lambda = 1.28$ . It means that

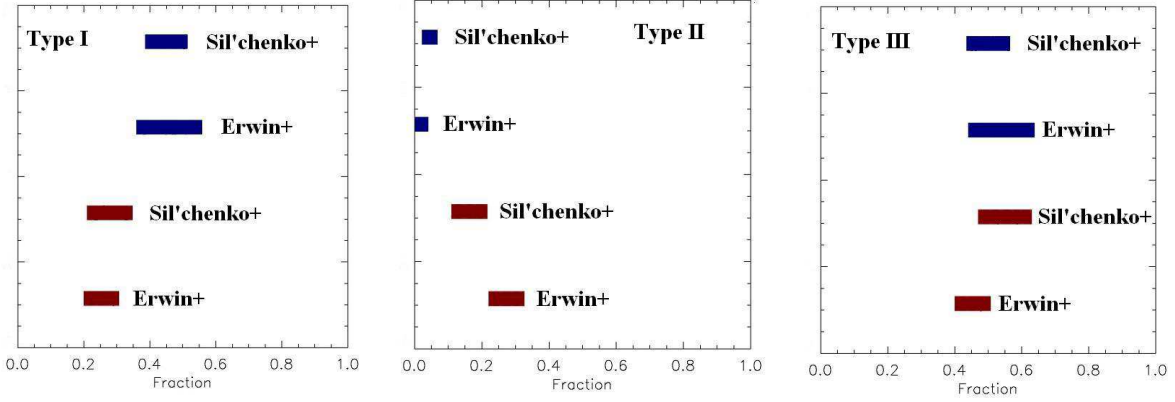


**Figure 7.** The statistics of the disk surface-brightness profile types in different environments: Type I in the left, Type II in the middle, and Type III in the right. The position along the abscissa marks the disk type fraction in a sample considered; the shift along the ordinate is arbitrary. The width of the bars indicates the estimate accuracy at one sigma level; the errors shown are derived from the binomial distributions. The red bars are plotted for the field, and blue bars are plotted for the clusters. The data are taken from: [Erwin et al. \(2012\)](#), marked by 'Erwin+', and [Sil'chenko et al. \(2018\)](#) and the present paper, marked by 'Sil'chenko+'.

the distributions are different at the 92% confidence level. The thickness distribution for the inner segments of Type-III disks in the isolated S0s reveals an additional strong peak at  $q \approx 0.42$  which is absent in the thickness distribution of the cluster Type-III disks. Meanwhile the thin disks similar to the inner segments of the Type-III disks in clusters are also present in some isolated S0s. We conclude that additional dynamical mechanisms affecting isolated S0s but not working in clusters may broaden the vertical structure of the stellar disks in our sample S0s.

Interestingly, in a few cases when we are able to estimate the thickness both for the inner and outer segments of the Type-III disks, they are similar: either both the inner and outer segments are thin, or both are thick (Fig. 9). Among four Type-III disks with the measured thicknesses of both segments, only NGC 1656 has the inner segment much thicker than the outer one,  $q_{inn} = 0.54 \pm 0.02$  vs  $q_{out} = 0.18 \pm 0.08$ ; evidently, it is the case of a pseudobulge with the exponential surface-brightness profile mimicking the anti-truncated disk. But otherwise the thickness of the Type-III disks in the isolated S0s keeps nearly constant beyond the breaks.

#### 4.4. Discussion: Particular mechanisms of S0 galaxy evolution in sparse environments

It is a well-established observational paradox: early-type galaxies in rarefied environments demonstrate signatures of interaction; minor merging, and/or gas accretion much more often than galaxies in clusters. The most prominent manifestation of this phenomenon is gas kinematics. For example, the volume-complete survey of nearby early-type galaxies ATLAS-3D revealed frequent misalignment of rotation planes between gas and stars just in S0 galaxies in loose groups and in the field while the Virgo cluster S0s, if they possess gas, showed always coupled rotation of stars and gas ([Davis et al. 2011](#)). We have fulfilled spectral study of the kinematics and stellar populations in the disks of quite isolated S0s selected from the same parent sample as the present study targets and have found ionized-gas presence in 75% of galaxies; the gas counterrotates the stars along the spectrograph slit in the half of the objects analyzed ([Katkov et al. 2014](#)). In addition, the disk stellar populations in the



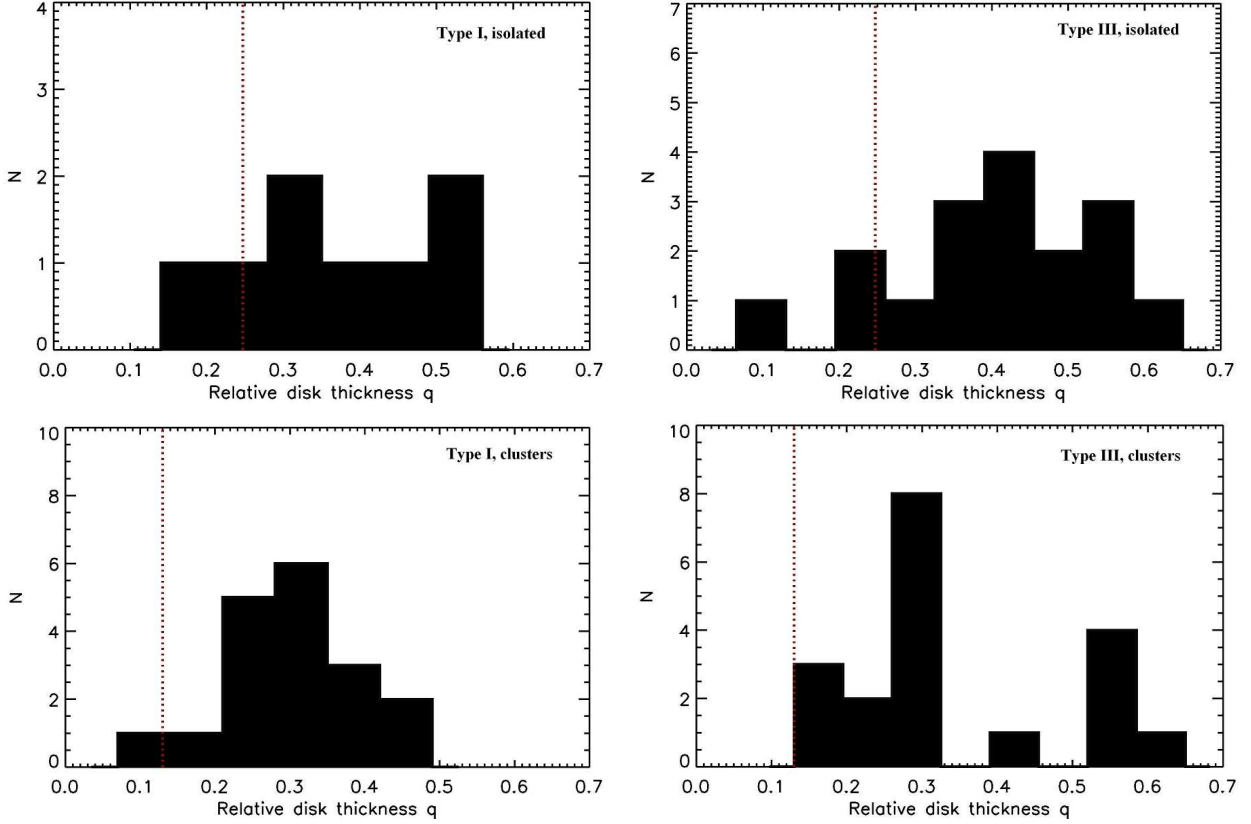


**Figure 8.** The distributions of the disk relative thickness for the Type-I disks (*left*) and for the inner segments of the Type-III disks (*right*). The vertical dotted red lines indicate the mean thicknesses of the inner segments of the Type-II disks. The upper row shows the results for the isolated S0s, and the bottom row – for the cluster S0s from our previous paper (Sil’chenko et al. 2018).

isolated S0s are in average younger than those of the S0 disks in groups and in clusters (Katkov et al. 2015).

Now we can look at the structure of the isolated S0s in comparison with the structure of the cluster S0s studied by us in the previous work (Sil’chenko et al. 2018). If we compare the bar frequency by using the data of Table 1 with the analogous Table from the paper by Sil’chenko et al. (2018), we can find that in the isolated S0s the bars are more frequent than in the cluster S0s:  $43\% \pm 8\%$  against  $27\% \pm 6\%$ . We may then suggest that the excess of bars in isolated S0s is caused by interactions. All thick inner segments of the Type-III disks in our isolated S0s,  $q > 0.43$ , are found in the galaxies with the bars or with signatures of recent minor merging (shells, blue compact inclusions). This fact can explain why we do not see such thick inner disks in the Type-III cluster S0s. Minor merging, especially dry minor merging, is a recognized dynamical mechanism to make stellar disks thick (Walker et al. 1996) and hot (Tapia et al. 2014); in addition, simulations demonstrate that just dry minor merging can produce antitruncated radial brightness distributions in the disks (Younger et al. 2007). Otherwise, the very presence of a strong bar can also produce an antitruncated density profile of a disk through enhanced radial migration (Herpich et al. 2017). These are possible extra-mechanisms that can work for the isolated galaxies and can thicken their stellar disks.

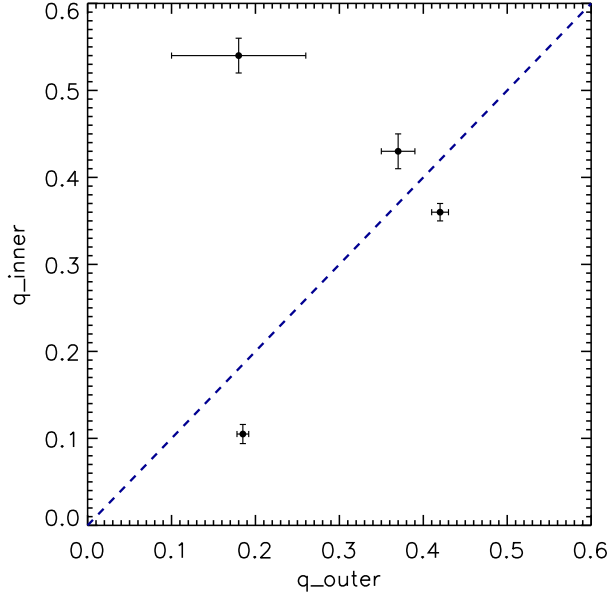


**Figure 9.** The comparison of the thicknesses of the inner and outer exponential segments for the Type-III disks of the isolated S0s.

However, the question remains to be open whether there is an evolutionary link between different types of the disk surface-brightness profiles. While the large-scale cosmological simulations imply transformations, say, of Type II into Type I and then perhaps into Type III (Ruiz-Lara et al. 2017), the observations of Type-III galaxies over a range of redshifts reveal quite stable structure parameters and scaling relations just for this disk type (Borlaff et al. 2018). Perhaps there is no evolutionary link between disk profile types, and we must search for initial conditions determining the disk type. Then the environment density is the most promising candidate for such conditions.

## 5. CONCLUSIONS

By undertaking two-band photometric observations at the Las Cumbres Observatory 1m-telescope network, we have studied large-scale disk structures for the sample of 42 isolated lenticular galaxies of the southern sky. In our sample we have identified all three types of the radial surface-brightness profiles – single-scale pure exponential (Type I), truncated (Type II), and antitruncated (Type III). The last are the most numerous: about a half of all lenticular galaxies have antitruncated radial brightness profiles, both in isolation and in clusters. The difference of the S0 disk radial structures between the galaxies evolving in visible isolation and those in clusters consists of a prominent presence of truncated stellar disks in the isolated S0s – slightly less than 20% isolated S0s demonstrate downward brightness breaks in their disks while in clusters such type of radial brightness profiles is almost absent. We have also measured the individual stellar-disk relative thicknesses for a significant part of our sample by exploring our original method applicable to the exponential, or partly exponential, disks with arbitrary orientation in the space. The thickness distributions seems to be different for the Type-III isolated S0s and S0s in clusters: in average, inner stellar disks of the Type-III isolated S0s are thicker. By summarizing the differences in the vertical and radial structures of the disks of lenticular galaxies in clusters and in isolation, we conclude that isolated S0s experience dynamical and structure evolution provoked by some mechanisms absent in clusters.

This work is based on the imaging data obtained with the LCO robotic telescope network. OKS and EMCh acknowledge the support from the Program of development of M.V. Lomonosov Moscow State University (Leading Scientific School 'Physics of stars, relativistic objects and galaxies'). AYK acknowledges support from the National Research Foundation of South Africa (NRF). We have made actively the usage of the HyperLEDA database (<http://leda.univ-lyon1.fr>). This research has made use of the NASA/IPAC Extragalactic Database (NED) which is operated by the Jet Propulsion Laboratory, California Institute of Technology, under contract with the National Aeronautics and Space Administration. For the purpose of our photometric calibration we have used SDSS/DR9 (Ahn et al. 2012) and Pan-STARRS1 data (Chambers et al. 2016; Flewelling et al. 2016). Funding for the SDSS-III has been provided by the Alfred P. Sloan Foundation, the Participating Institutions, the National Science Foundation, and the U.S. Department of Energy Office of Science. The SDSS-III Web site is <http://www.sdss3.org/>. SDSS-III is managed by the Astrophysical Research Consortium for the Participating Institutions of the SDSS-III Collaboration including the University of Arizona, the Brazilian Participation Group, Brookhaven National Laboratory, Carnegie Mellon University, University of Florida, the French Participation Group, the German Participation Group, Harvard University, the Instituto de Astrofísica de Canarias, the Michigan State/Notre Dame/JINA Participation Group, Johns Hopkins University, Lawrence Berkeley National Laboratory, Max Planck Institute for Astrophysics, Max Planck Institute for Extraterrestrial Physics, New Mexico State University, New York University, Ohio State University, Pennsylvania State University, University of Portsmouth, Princeton University, the Spanish Participation Group, University of Tokyo, University of Utah, Vanderbilt University, University of Virginia, University of Washington, and Yale University. The Pan-STARRS1 Surveys (PS1) and the PS1 public science archive have been made possible through contributions by the Institute for Astronomy, the University of Hawaii, the Pan-STARRS Project Office, the Max-Planck Society and its participating institutes, the Max Planck Institute for Astronomy, Heidelberg and the Max Planck Institute for Extraterrestrial Physics, Garching, The Johns Hopkins University, Durham University, the University of Edinburgh, the Queen's University Belfast, the Harvard-Smithsonian Center for Astrophysics, the Las Cumbres Observatory Global Telescope Network Incorporated, the National Central University of Taiwan, the Space Telescope Science Institute, the National Aeronautics and Space Administration under Grant No. NNX08AR22G issued through the Planetary Science Division of the NASA Science Mission Directorate, the National Science Foundation Grant No. AST-1238877, the University of Maryland, Eotvos Lorand University (ELTE), the Los Alamos National Laboratory, and the Gordon and Betty Moore Foundation.

*Facilities:* LCO, SDSS, Pan-STARRS, NED, HyperLEDA

## APPENDIX

### A. OBSERVATIONAL DETAILS

**Table 5.** The galaxies studied photometrically with the LCO network.

Galaxy	Telescope	Date	Band	Exposure, sec	Seeing, ''
ESO 003-G001	Siding Spring, 1m0-03	20170901	g	800x3	2.8
ESO 003-G001	Siding Spring, 1m0-03	20170901	r	600x3	2.5
ESO 040-G002	Cerro Tololo, 1m0-05	20180220	g	800x3	1.8
ESO 052-G014	Siding Spring, 1m0-11	20170901	g	800x3	1.9
ESO 052-G014	Siding Spring, 1m0-11	20170901	r	600x3	1.8
ESO 069-G001	Siding Spring, 1m0-03	20170901	g	800x3	2.4
ESO 069-G001	Siding Spring, 1m0-03	20170901	r	600x3	2.4
ESO 235-G051	SAAO 1m0-12	20170926	g	800x3	1.3
ESO 235-G051	SAAO 1m0-12	20170926	r	600x3	1.1
ESO 265-G033	Cerro Tololo, 1m0-04	20160410	g	800x3	1.8
ESO 265-G033	Cerro Tololo, 1m0-04	20160410	r	600x3	1.3
ESO 269-G013	Cerro Tololo, 1m0-09	20160408	g	800x3	1.7
ESO 269-G013	Cerro Tololo, 1m0-09	20160408	r	600x3	1.4
ESO 274-G017	Siding Spring, 1m0-03	20170920	g	800x3	1.8
ESO 274-G017	Siding Spring, 1m0-03	20170920	r	600x3	1.8
ESO 316-G013	SAAO 1m0-10	20171224	g	800x3	1.6
ESO 316-G013	SAAO 1m0-10	20171224	r	600x3	1.9
ESO 324-G029	Cerro Tololo, 1m0-04	20160408	g	800x3	1.8
ESO 324-G029	Cerro Tololo, 1m0-04	20160408	r	600x3	1.9
ESO 446-G049	Cerro Tololo, 1m0-04	20180120	g	800x3	1.9
ESO 446-G049	Cerro Tololo, 1m0-04	20180120	r	600x3	1.7
ESO 469-G006	Cerro Tololo, 1m0-04	20160807	g	800x3	1.9
ESO 469-G006	Cerro Tololo, 1m0-04	20160807	r	600x3	1.8
ESO 486-G038	Siding Spring, 1m0-03	20170901	g	800x3	2.2
ESO 486-G038	Siding Spring, 1m0-03	20170901	r	600x3	2.2
ESO 496-G003	Cerro Tololo, 1m0-05	20171223	g	800x3	1.5
ESO 496-G003	Cerro Tololo, 1m0-05	20171223	r	600x3	1.4
ESO 506-G011	Cerro Tololo, 1m0-09	20160409	g	800x3	1.6
ESO 506-G011	Cerro Tololo, 1m0-09	20160409	r	600x3	1.5
ESO 508-G033	Cerro Tololo, 1m0-09	20160408	g	800x3	1.5

*Table 5 continued on next page*

**Table 5** (*continued*)

Galaxy	Telescope	Date	Band	Exposure, sec	Seeing,"
ESO 508-G033	Cerro Tololo, 1m0-09	20160408	r	600x3	1.8
ESO 545-G040	Siding Spring, 1m0-03	20170901	g	800x2	2.1
ESO 545-G040	Siding Spring, 1m0-03	20170901	r	600x3	2.05
ESO 563-G024	SAAO 1m0-10	20171215	g	800x3	1.7
ESO 563-G024	SAAO 1m0-10	20171215	r	600x3	1.4
ESO 603-G029	Cerro Tololo, 1m0-05	20171215	g	800x3	1.9
ESO 603-G029	Cerro Tololo, 1m0-05	20171215	r	600x3	1.6
IC 276	Siding Spring, 1m0-11	20170901	g	800x2	2.1
IC 276	Siding Spring, 1m0-11	20170901	r	600x2	1.9
IC 537	SAAO, 1m0-12	20180221	g	800x3	2.4
IC 537	SAAO, 1m0-12	20180221	r	600x2	2.3
IC 537	Cerro Tololo, 1m0-04	20180321	g	800x3	2.3
IC 4913	Cerro Tololo, 1m0-04	20160410	g	800x3	1.5
IC 4913	Cerro Tololo, 1m0-04	20160410	r	600x3	1.4
NGC 270	McDonald Observatory, 1m0-08	20170831	g	800x3	1.7
NGC 270	McDonald Observatory, 1m0-08	20170831	r	600x3	1.5
NGC 324	Cerro Tololo, 1m0-04	20170923	g	800x3	1.7
NGC 324	Cerro Tololo, 1m0-04	20170923	r	600x3	1.5
NGC 1656	Siding Spring, 1m0-11	20170925	g	800x3	3.1
NGC 1656	Siding Spring, 1m0-11	20170925	r	600x3	2.8
NGC 4087	Cerro Tololo, 1m0-05	20171223	g	800x3	1.6
NGC 4087	Cerro Tololo, 1m0-05	20171223	r	600x3	1.3
NGC 4878	McDonald Observatory, 1m0-08	20180220	g	800x2	2.7
NGC 4878	McDonald Observatory, 1m0-08	20180321	g	800x3	1.7
NGC 4878	McDonald Observatory, 1m0-08	20180321	r	600x3	1.5
NGC 5890	McDonald Observatory, 1m0-08	20180321	g	800x3	2.1
NGC 5890	McDonald Observatory, 1m0-08	20180321	r	600x3	1.6
NGC 6014	Cerro Tololo, 1m0-05	20180321	g	800x3	1.9
NGC 6014	Cerro Tololo, 1m0-05	20180321	r	600x3	1.4
NGC 7007	Siding Spring, 1m0-03	20170901	g	800x3	2.4
NGC 7007	Siding Spring, 1m0-03	20170901	r	600x3	2.2

*Table 5 continued on next page*

**Table 5** (*continued*)

Galaxy	Telescope	Date	Band	Exposure, sec	Seeing,"
NGC 7208	Cerro Tololo, 1m0-09	20160808	g	800x3	1.9
NGC 7208	Cerro Tololo, 1m0-09	20160808	r	600x3	2.0
PGC 11756	McDonald Observatory, 1m0-08	20170831	g	800x3	1.6
PGC 11756	McDonald Observatory, 1m0-08	20170831	r	600x3	1.5
PGC 16688	Cerro Tololo, 1m0-05	20170925	g	800x3	1.6
PGC 16688	Cerro Tololo, 1m0-05	20170925	r	600x3	1.6
PGC 34728	Siding Spring, 1m0-03	20171223	r	600x3	1.9
PGC 35771	Cerro Tololo, 1m0-09	20160410	g	800x3	2.5
PGC 35771	Cerro Tololo, 1m0-09	20160410	r	600x3	2.0
PGC 46474	Cerro Tololo, 1m0-04	20180319	g	800x3	1.6
PGC 46474	Cerro Tololo, 1m0-04	20180319	r	600x3	1.5
PGC 52002	Cerro Tololo, 1m0-05	20180321	g	800x3	1.4
PGC 52002	Cerro Tololo, 1m0-05	20180321	r	600x3	1.4
PGC 58114	McDonald Observatory, 1m0-08	20180321	g	800x3	1.5
PGC 58114	McDonald Observatory, 1m0-08	20180321	r	600x3	1.5
PGC 63536	SAAO 1m0-12	20180320	g	800x3	2.1
PGC 63536	SAAO 1m0-12	20180320	r	600x3	2.1
PGC 68401	Cerro Tololo, 1m0-04	20160808	g	800x3	1.9
PGC 68401	Cerro Tololo, 1m0-04	20160808	r	600x3	1.8
UGC 3097	SAAO 1m0-10	20171210	g	800x2	2.5
UGC 3097	SAAO 1m0-10	20171224	g	800x3	1.8
UGC 3097	SAAO 1m0-10	20171224	r	600x3	1.5
UGC 5745	Cerro Tololo, 1m0-04	20180220	g	800x3	1.9
UGC 5745	Cerro Tololo, 1m0-04	20180220	r	600x3	1.7

## REFERENCES

- Ahn, C. P., Alexandroff, R., Allende Prieto, C., Anderson, S. F., Anderton, T., et al., 2012, *ApJS*, 203, A12.
- Bekki, K., Couch, W. J., 2011, *MNRAS*, 415, 1783
- Borlaff, A., Eliche-Moral, M. C., Rodr ´ Iguez-P´erez, C., Querejeta, M., Tapia, T., et al. 2014, *A&A*, 570, A103
- Borlaff, A., Eliche-Moral, M. C., Beckman, J. E. et al. 2018, *A&A*, 615, A26
- Brown, T. M., Baliber, N., Bianco, F. B., Bowman, M., Burleson, B., et al. 2013, *PASP*, 125, 1031
- Byrd, G., Valtonen, M., 1990, *ApJ*, 350, 89
- Cappellari, M., Emsellem, E., Krajnovic, D., et al., 2011, *MNRAS*, 413, 813

- Chambers, K. C., Magnier, E. A., Metcalfe, N., Flewelling, H. A., Huber, M. E., et al., 2016, ArXiv: 1612.05560
- Chudakova, E. M., 2019, *Astron. Reports*, 63, 353
- Chudakova, E. M., Sil'chenko, O. K. 2014, *Astron. Reports*, 58, 281; ArXiv: 1410.6713
- Clarke, A. J., Debattista, V. P., Roskar, R., Quinn, T. 2017, *MNRAS*, 465, L79
- Comerón, S., Salo, H., Knapen, J. H. 2018, *A&A*, 610, A15
- Cowie L.L., Songaila A., 1977, *Nature*, 226, 501
- Davis, T. A., Alatalo, K., Sarzi, M., Bureau, M., Young, L. M., et al., 2011, *MNRAS*, 417, 882
- Erwin, P., Beckman, J. E., Pohlen, M. 2005, *ApJL*, 626, L81
- Erwin, P., Pohlen, M., Beckman, J. E. 2008, *AJ*, 135, 20
- Erwin, P., Gutiérrez, L., Beckman, J. E. 2012, *ApJL*, 744, L11
- Flewelling, H. A., Magnier, E. A., Chambers, K. C., Heasley, J. N., Holmberg, C., et al., 2016, ArXiv: 1612.05243
- Freeman, K. C. 1970, *ApJ*, 160, 767
- Gunn, J. E., Gott, J. R., III, 1972, *ApJ*, 176, 1
- Gutiérrez, L., Erwin, P., Aladro, R., Beckman, J. E. 2011, *AJ*, 142, A145
- Herpich, J., Stinson, G. S., Rix, H.-W., Martig, M., Dutton, A. A. 2017, *MNRAS*, 470, 4941
- Hubble, E. 1926, *ApJ*, 64, 321
- Icke, V., 1985, *A&A*, 144, 115
- Jordi, K., Grebel, E. K., Ammon, K. 2006, *A&A*, 460, 339
- Karachentsev, I. D., Makarov, D. I., Karachentseva, V. E., Melnyk, O. V. 2011, *Astrophys. Bull.*, 66, 1
- Katkov, I. Yu. 2014, PhD Thesis.
- Katkov, I. Yu., Sil'chenko, O. K., Afanasiev, V. L., 2014, *MNRAS*, 438, 2798
- Katkov, I. Yu., Kniazev, A. Yu., Sil'chenko, O.K. 2015, *AJ*, 150, A124
- Larson, R. B., Tinsley, B. M., Caldwell, C. N., 1980, *ApJ*, 237, 692
- Lauberts, A., Valentijn, E. A., 1989, *The Messenger*, 56, 31
- Makarov, D., Karachentsev, I. 2011, *MNRAS*, 412, 2498
- Makarov, D., Prugniel, P., Terekhova, N., Courtois, H., Vauglin, I., 2014, *A&A*, 570, A13
- Mosenkov, A. V., Sotnikova, N. Ya., Reshetnikov, V. P. 2010, *MNRAS*, 401, 559
- Mosenkov, A. V., Sotnikova, N. Ya., Reshetnikov, V. P., Bizyaev, D. V., Kautsch, S. J. 2015, *MNRAS*, 451, 2376
- Moore, B., Katz, N., Lake, G., Dressler, A., Oemler, A., 1996, *Nature*, 379, 613
- Pohlen, M., Trujillo, I. 2006, *A&A*, 454, 759
- Pranger, F., Trujillo, I., Kelvin, L. S., Cebrián, M. 2017, *MNRAS*, 467, 2127
- Quilis, V., Moore, B., Bower, R., 2000, *Science*, 288, 1617
- Ruiz-Lara, T., Few, C.G., Florido, E., Gibson, B.K., Pérez, I., Sánchez-Blázquez, P., 2017, *A&A*, 608, A126
- Sil'chenko, O. K., Burenkov, A. N., Vlasjuk, V. V. 1998, *New Astron.*, 3, 15
- Sil'chenko, O. K., Koposov, S. E., Vlasjuk, V. V., Spiridonova, O.I. 2003, *Astron. Reports*, 47, 88
- Sil'chenko, O. K., Kniazev, A. Yu., Chudakova, E. M. 2016, *Astron. Reports*, 60, 73
- Sil'chenko, O. K., Kniazev, A. Yu., Chudakova, E. M. 2018, *AJ*, 156, A118
- Spitzer, L., Jr., Baade, W., 1951, *ApJ*, 113, 413
- Tapia, T., Eliche-Moral, M. C., Querejeta, M., et al. 2014, *A&A*, 565, A31
- Van der Kruit, P. C., Searle, L. 1981, *A&A*, 95, 105
- Walker, I. R., Mihos, J. Ch., Hernquist, L., 1996, *ApJ*, 460, 121
- Younger, J. D., Cox, T. J., Seth, A. C., Hernquist, L. 2007, *ApJ*, 670, 269